A 4D Ultrasound Tomography for Industrial Process Reactors Investigation

Panagiotis Koulountzios, Tomasz Rymarczyk and Manuchehr Soleimani

***Abstract*—A volumetric ultrasound tomography (UST) system and method are established for industrial process applications. A two-plane ring-array UST system is developed for 3D imaging of the process under test. Such a 3D system allows capturing axial variations, which is not possible in 2D or 2.5D imaging. A ray-voxel intersection method is used to create the sensitivity matrix needed for the 3D or 4D image reconstruction. Acquiring and processing time series data lead to 4D imaging, generating dynamical volumetric image by using a time correlative total variation (TV) algorithm. The 3D forward model using the ray propagation model offers a computationally efficient tool for modelling the measurement process in UST and is used for image reconstruction. In combination with the advanced 4D TV algorithm, high-quality information is gained from time and space. At first, the 3D imaging methodology was tested and verified using static objects. Secondly, 4D imaging was investigated by using a moving rod in an experimental tank. The system was then implanted to carry out dynamical process monitoring, imaging 4D crystallisation process. Finally, the results are evaluated using quantitative image evaluation in 3D mode and process dynamics in 4D imaging mode.**

***Index Terms*— ultrasound tomography, process tomography, 4D imaging, crystallisation process tomography**

I. Introduction

ULTRASOUND tomography (UST) has been studied and developed in 2D and 3D setups for various medical and industrial process imaging applications. Volumetric (3D) industrial tomography is more informative than the 2D setups, as it provides full information from the three-dimensional region-of-interest (ROI) using modalities such as electrical impedance tomography (EIT), electrical capacitance tomography (ECT), X-ray computed tomography (XCT) and others [1]–[5]. Volumetric imaging in all the above modalities provides a more detailed understanding of the industrial process under investigation. The 2D imaging is always an approximation to the actual physical scenario. Considering full geometrical conditions allows producing high-quality images with more information. The benefits of 3D imaging were displayed on industrial process tomography against traditional 2D and 2.5D imaging in [6]. The 2.5D imaging is a prior to 3D technique and is conducted by interpolating independent 2D images into a 3D volume, being considered as an approximation method.

UST has been studied in 3D fashion in transmission and multi-modality techniques, mainly for medical applications [7]–[10]. Medical applications of the UST [11]–[13] have been very promising in breast cancer imaging, where the advanced 3D full-waveform inversion (FWI) or other computationally complex algorithms [14]–[16] can provide images reaching the quality standards of XCT or to Magnetic Resonance Imaging (MRI). Aiming at high spatial resolution, medical systems require not only heavy computational reconstruction algorithms but also many sensors (for example, 1000 transducers). This leads to time-consuming data collection and eventually, imaging is too slow and not suitable for agile industrial applications. On the other hand, almost all newly developed UST systems for industrial applications are based on 2D imaging [17]–[20]. UST industrial applications are mainly focused on the liquid transportation pipelines and multiphase flow monitoring [21]–[23]. USCT also finds great need in and liquid/ gas flow imaging, which is a process widespread in the chemical, oil and gas, pharmaceutical and energy industries [24]–[26]. However, the significant need for volumetric monitoring in industrial process imaging leads to new incorporated 3D developments. Regarding the high temporal changes of the live industrial processes, developing a fast-imaging system is crucial. Therefore, the number of sensors and the form of the acquired data are designed optimally for high temporal imaging, satisfying the spatial resolution requirements.

Early tomographic developments have been focused on enhancing the spatial resolution of single-frame data. Conventional single-step reconstruction algorithms are based on single frame data. However, in a real-time environment, multiple data-frames needs to be processed. In that case, dynamic regularization algorithms, accounting for temporal resolution, needs to be addressed. First attempts of such algorithms were made in 2D tomographic problems [27], [28]. Nevertheless, the need for established 3D systems drove to the development of temporal 4D regularization algorithms [1], [5], [24]–[31].

This work provides a method for 3D and 4D imaging for UST that fulfills the needs of industrial process tomography. A 3D transmission UST was developed, using the first-arrival pulse's time-of-flight and incorporating multiple ring arrays. UST in transmission mode can be considered as a hard-field tomography, thereafter an improved ray-voxel intersection adjustment is proposed similar to those implemented in XCT. Ultrasound transmission tomography involves some ill

M Soleimani and P Koulountzios are with Engineering Tomography Laboratory (ETL), Department of Electronic and Electrical Engineering, University of Bath, Bath BA2 7AY, United Kingdom. T Rymarczyk is with Research & Development Centre Netrix S.A., Wojciechiwska 31, 20-704 Lublin, Poland.

This work was supported by the European Union's Horizon 2020 research and innovation program under the Marie Skłodowska-Curie Grant 764902.

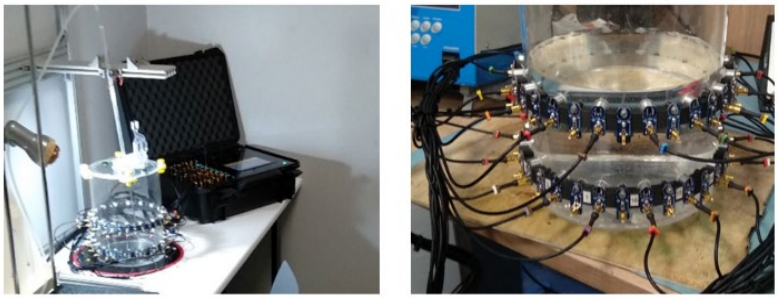

(a)

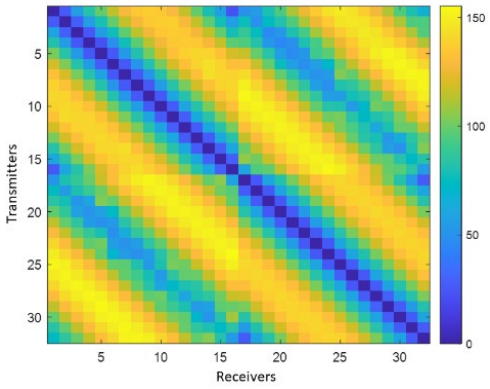

(b)

Fig. 1. (a) UST system and sensors attached in the 20cm-diameter tank and a zoomed view of the two layers of the 16 sensors each. **(b)** 1024 TOF background measurements coming from 32 sensors in the two-ring array.

condition inverse problem, requiring a regularization-based image reconstruction method. The work contributes to the field of UST as it is the first deployment of a 3D UST system for process reactors monitoring. Moreover, this work's additional contribution is the application of the 4D regularization algorithm in 3D UST system, as it offers temporally correlated dynamical imaging. 4D imaging is accomplished via a 4D Total variation algorithm in a 3D UST system.

This paper is organised as follows: Section II describes the volumetric UST system and 4D regularization algorithm. Section III is dedicated to several static and dynamical experiments, including the crystallisation process. Finally, the conclusions are drawn in Section IV.

II. Volumetric UST System and Method

A. UST Hardware System

Fig. 1(a) shows the ultrasonic tomograph with 32 channels where the travel time data can be collected between two rings of 16 sensors each. Sensors can be used as transmitters or receivers. In total, 1024 measurements are possible, with the exciting sensor's received signal to be considered null. Fig. 1(b) shows the time-of-flight (TOF) data for a homogeneous liquid background, a 1024 TOF data values coming from 32 excitations, with 32 recordings per excitation. The data were displayed in an image form. Every image's row account for a different excitation during every column for another recording. The zero diagonal line indicates the zero values of the self-measurements, namely the measurements coming from the same sensor as the excitation sensor.

Furthermore, with a closer look at the first 32 recordings, which account for the first excitation (first row), it can be noticed that the first 16 values are related to the inter-plane excitation and the rest 16 to the same plane excitation, as the later 16 TOF values seem to be higher. Thus, there is a noticeable pattern on this image that can distinguish between quadrants. This TOF data's pattern exists due to the topology of sensors and the excitation sequence and can describe the tomographic setup. The inter-plane data plays an important role in volumetric image reconstruction, providing an axial resolution that may not be possible in typical 2.5D imaging.

The UST hardware system has a configurable range of settings. It can provide raw full-waveform data (full-waveform mode) or processed TOF and amplitude values of the travel-time pulse (transmission mode). It also offers adjustable features on the acquisition's wavelength range. These settings are adapted to the needs of the specific process as they significantly affect the data acquisition process. For example, the transmission mode is a lot less time-consuming than the full-waveform mode due to the size of the processed data. Therefore, the settings adjustment depends on the investigation process and the range of measured data. Regarding real-time monitoring, the tomograph is preferably set to transmission mode. Table 1 displays the system's parameters.

The tomograph in transmission mode measures pulse's TOF and amplitude. The device automatically finds the minimum and maximum values of the signal, based on which it converts the percentage value to the numerical value of the ADC converter. The comparator threshold works only in the signal area beyond the value specified by the following parameter. The moment the signal exceeds the comparator threshold, the

Table 1. UST system's settings.

Parameter	Value
Transducers' frequency	400 kHz
Number of pulses	6
Supply voltage	+72/−72 V
Pull to the ground after extortion	ENABLE
GAIN first stage	45.2 dB
GAIN the second stage	1 *v/v*
Analog filter	Band-pass, fc=350 kHz (center freq.), fb=200kHz (bandwidth)
Parameter filtering	HI
Number of channels	32
Functionality mode	Transmission
Comparator threshold	5.11%

measurement window opens. The most considerable amplitude value from this area is stored and processed to compute its time-of-flight.

The developed UST system has been described priorly in [32]. The hardware design provides 84 measurement channels for possible use. Each sensor has its signal conditioning and measurement circuit, so all measurements for each excitation can be done simultaneously. The designed measuring cards have a maximum sampling rate of 4MBPS per channel. Each channel is equipped with a separate generator of AC rectangular waveforms with amplitude up to 144Vp-p and an instantaneous current capacity of 3A. It is possible to sample the analogue signal on all channels simultaneously. Three eight-order filters are built into each channel for effective harmonic filtering, triggered by analogue keys. The 350kHz band-pass filter with 200kHz centre frequency and 200kHz bandwidth for 300kHz and 400kHz transducers was used. The unit has two-stage gain control on each channel. The first stage from +7.5dB to +55.5dB (AD8331), while the second stage from +6dB to +36dB (6 settings - STM32's built-in PGA). Each channel is shielded, so the channels are very well isolated from each other. The device's implemented signal filtering is particularly important. Built-in filters allow to get rid of harmonics of other frequencies, but they also affect the signal strength. In overall the device's temporal resolution is 4fps. The measurement system uses MCUSD11A400B11RS ultrasonic sensors with frequency 400kHz, +/- 16kHz, diameter 11mm, a material made of aluminum, input voltage 300Vp-p, directivity (-3dB) 7° +/- 2°, operating temperature -20° C to 80° C. For each transmitter, an excitation of 5 cycles (tone burst) pulse takes place. However, they have a slightly smaller wave propagation angle compared to 40kHz sensors. As a result, the wave period is much smaller, so that the TOF measurement error is almost 10 times smaller. Therefore, 400kHz transmitters are the most accurate and are suitable for transmission measurements.

In addition, single excitation reference measurements were carried out to measure the width of wave propagation for a 400kHz transducer. For this purpose, 32 measuring points were placed at appropriate intervals around the circumference of the tank. The results of the measurements are shown in Table 1 and

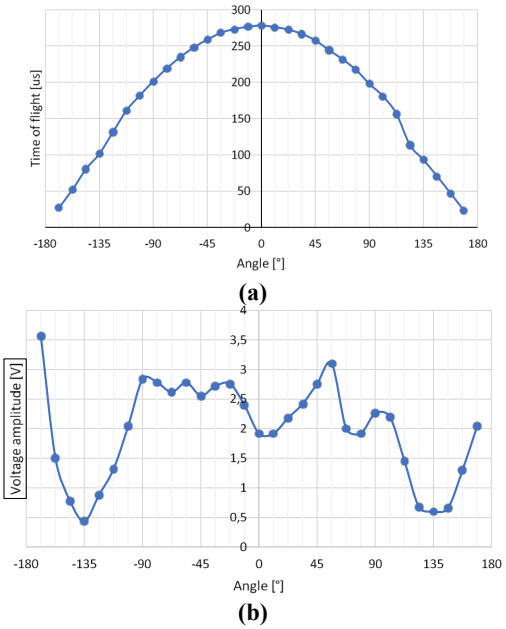

Fig. 2. 400 kHz transducers (a) TOF characteristics, (b) amplitude characteristics.

the characteristics in Fig. 2. A high keying voltage is required to achieve good quality measurements. The amplitude measurements address that the transducer works optimally in the range of +/- 90 degrees. Above that, its signal is much weaker. The TOF data seem to be reliable, and measurement errors are minimal.

The proposed reconstruction method uses the subtraction of experimental data and reference data. Such methods are categorised as "difference imaging" and constitute relative reconstructions of the ROI due to the subtraction of the actual experimental measurement from the background measurement. Incorporating such logic focuses on the changes described between the prior (background) and later phase (experiments). TOF measurement data result from subtracting the background from the full data, defining the travel-time delays in microseconds (μs), as shown in eq. (1).

$$\delta T = T_{full} - T_{back} \tag{1}$$

B. 3D Forward Model

A 3D ultrasound transmission tomography method was developed and applied to this work based on the time-of-flight of the first arrival pulse, whose trajectory is assumed as a straight line. The travel-time reconstruction method was used accounting for time delays resulting from the subtraction of TOF reference data and TOF experimental data. Considering high emission frequency, the ray trajectory can be solved by:

$$\frac{d}{dl}\left(\frac{1}{c}\frac{d\boldsymbol{x}}{dl}\right) = \frac{1}{c^2}\nabla c \tag{2}$$

where l is the arc length along the ray trajectory, $\boldsymbol{x}$ is the position vector, and c is the speed of sound [33]. With the position of the source and take-off angle of the source, one can specify the ray path. Assuming a uniform travel-time delays

model that only depends on the depth, one can use a simplified method for the wave propagation based on the ray-approximation approach:

$$\delta T = \int_{ray} \delta s(x)\, dl \tag{3}$$

where the above integral is based on a single ray path, δs denotes the "travel-time delays" distributions in μs scale, and finally, δT gives the "travel-time delay" of the pulse. The term "travel-time delays" defines the time difference between a propagating in the reference medium signal and a propagating experimental signal. Assuming that the ray path is sensitive to a small travel-time perturbation, the perturbation in travel-time is given by the path integral of the average travel-time perturbation along the ray. It will allow a linear inversion algorithm based on a linear forward model. A linear method requires data from a background state (prior state) and a state where the domain has changed (experimental state). For a linearised forward problem, the above equation (3) can be expressed as:

$$\delta T = A\, \delta s \tag{4}$$

where δs is differences in arrival time, A is the modelling operator which describes the sensitivity distribution, and δT is the travel-time distribution.

For solving the 3D forward problem of eq. (4), a domain needs to be addressed. Then, the software for 3D UST sensitivity matrix computation is based on the ray-voxel intersection algorithms of tray-tracing methods [34], [35], [36]. Thus, by calculating the intersection region, the weighted values can be assigned. In the specific experimental cases, the sensor rings have a perimeter of 200-mm, and they are positioned in layers of a 70-mm distance. A (32x32) spatial resolution was applied for the cross-sectional planes of a 200-mm edge. For the z-axis, a study was followed to compare and provide a well-arranged discretisation, following the cross-sectional planes' sensitivity distribution. Finally, a (32x32x4) cuboid voxels grid was used. Comparing the sensitivity distributions between different cases of different discretisation along the z-axis, the proposed seems to overcome sparsity and be superior. A ray-based algorithm is computationally efficient in linear image reconstruction, especially FWI, making it a good candidate for industrial application. The matrix A can be pre-calculated and evaluated before it can be used for the image reconstruction process.

C. Optimised ray-voxel intersection

An optimised ray-voxel intersection method was developed for assigning values to the sensitivity matrix. In the pre-developed 2D UST algorithm, the pixel was considered circular instead of square. The inscribed circle of a pixel defines the circular pixel. Thus, the imaging software becomes much faster, particularly important in cases where "online" imaging is needed [37]. Regarding this modification, an approximation of this method for 3D models was developed. Prior studies have shown the efficiency of this concept in 3D problems [38]. Furthermore, the voxel has been treated as an inscribed sphere of a voxel rather than as a cube. Thus, the method's main objective is to compare the distance from the ray to the voxel's center, with the voxel's radius. Subsequently, only one task needs to be executed instead of four complicated ones, leading to less complexity. Therefore, the distance of the ray to the voxel's center is computed, as shown in eq. (5).

$$d = \frac{\|(v_1 - v_2) \times (pt - v_2)\|}{\|v_1 - v_2\|} \tag{5}$$

where pt, v_1 and v_2 are the three-dimensional coordinates of the point, one vertex of the line, and a second vertex of the line, respectively. The symbol x defines the cross-product equation. Then the distance, d, is compared to a fixed value, which usually is the radius, r, of the spherical voxel [39]. By increasing the intersection criterion value, the calculated rays turn to "thick lines" tackling sparsity that might be introduced [40]. To enhance the sensitivity distribution and subsequently the inversion's outcomes, we chose to apply a "thick lines" model. Such a model is more realistic to the real setup because it accounts for the piezoelectric transducers' characteristics.

Rymarzyck et al. have presented a method of incorporating smoother sensitivity distribution by using the circumscribed sphere's radius instead of using the inscribed spheres' radius of the voxel [41]. The circumscribed sphere's radius represents half of the diagonal value of the voxel. The diagonal, dg, is calculated by equation below:

$$dg = \sqrt{(r)^2 + (r)^2} \tag{6}$$

This approach works better than the previous approach, which used the inscribed circle to the voxel. Moreover, it proved to offer less sparsity in the outcomes. The method was tested in a cubic voxels grid. However, in the specific case of (32x32x4) resolution, the grid consists of spheroid voxels. A spheroid has not had a unique radius value. Instead, it can be defined by two radii. The longer radius is called the semi-major axis, and the shorter radius is called the semi-minor axis. Therefore, we proposed 2 radii to be used in the mathematical function of the algorithm to calculate the diagonal, dg.

$$r_1 = \frac{vl_1}{2}, \qquad where \quad vl_1 = \frac{200}{32}\text{mm} \tag{7}$$

$$r_2 = \frac{vl_2}{2}, \qquad where \quad vl_2 = \frac{70}{4}\text{ mm} \tag{8}$$

So, eq. (6), in respect of eq. (7) and (8), becomes:

$$dg = \sqrt{(r_1)^2 + (r_2)^2} \tag{9}$$

where dg is the distance that defines the radius of the circumscribed spheroid on cuboid voxel? Elements of matrix A can be produced by the ratio of the radius length to the distance from the ray to the center of the voxel as per eq. (10).

$$A_{i,j} = \begin{cases} 0, & for\ d > dg \\ \sqrt{1 - \left(\frac{d}{R}\right)^2}, & for\ d \le dg \end{cases} \quad (10)$$

Eq. (10) includes the distance criterion, which defines the ray-voxel intersection. So, for voxels that are not intersected with the ray, zero values are assigned.

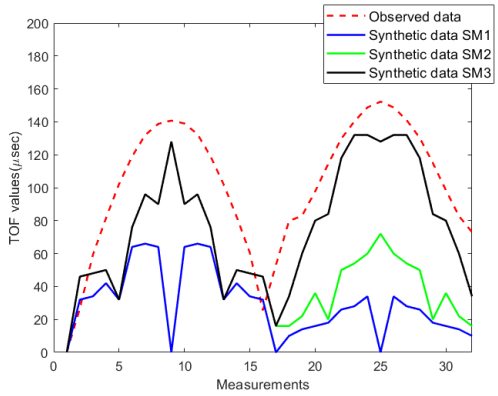

Fig. 3. Observed and synthetic TOF data plotted together with simulated linear forward model.

For every other voxel the assigned value is described as a weighted value proportional to the amount of the ray that intersects the voxel's area. For the computation regarding rays on a single plane and for inter-planar rays, the corresponding radius' combination between (r_1, r_1) and (r_1, r_2) were used. Thus, the sensitivity matrix contains weighted values which define the regional sensitivity according to the effect of rays on every voxel of the ROI.

To evaluate the proposed methodology, the values of the experimental reference measurement data is compared with the synthetic background data produced by three generated sensitivity matrices based on different methodology. At first, a method which uses as an intersection convergence criterion the inscribed sphere's radius is noted as "SM1"; then a sensitivity matrix that uses the circumscribed sphere's radius is noted as "SM2"; and finally, the sensitivity matrix which incorporates both radii to calculate dg for the interplanar computations is noted as "SM3". All three matrices are multiplied by a unity vector to produce the so-called "synthetic" data. The first 32 values of these data and the experimental reference data are plotted together in Fig. 3. It represents how well each matrix can produce data from a measurement of uniform background (for example, water background). As it can be seen, the "SM3" provides a better approximation against the real measured data.

D. Inverse problem with 4D regularization

In dynamical 3D imaging, the image reconstruction process deals with many frames of data and images. Certain information in x,y,z space can be temporally regularised, providing 4D imaging. We use a 4D total variation (TV) algorithm proven very successful in various other imaging modalities [24]–[26]:

$$arg\min_{\delta s} \left\|\nabla_{x,y,z}\delta s\right\|_1 + \left\|\nabla_t \delta s\right\|_1 \quad \text{s.t.} \quad \left\|\tilde{A}\delta s - \delta T\right\|_2^2 \le e \quad (11)$$

where spatial and temporal TV-based regularization terms (first two terms in eq. 10) and the Δs represents a 4D travel-time delays distribution and $\tilde{A}$ represents the linear sensitivity matrix, and e represents the expected noise level in the measuring system and model uncertainty.

The Split Bregman (SB) method [42], [43] will be used to solve the constrained optimisation problem of equation (10). Using the Bregman iteration can lead to an iterative scheme:

$$\delta s^{k+1} = arg\min_{\Delta s} \left\|\nabla_{x,y,z}\delta s\right\|_1 + \left\|\nabla_t \delta s\right\|_1 + \sum_{i=1}^{I} \frac{\mu}{2} \left\|\tilde{A}\delta s - \delta T^k\right\|_2^2 \quad (12)$$

$$\delta T^{k+1} = \delta T^k - \tilde{A}\delta s^{k+1} + \Delta\delta, \quad (13)$$

Including auxiliary variables in the SB algorithm allows splitting L1- and L2-functional to easily solve them in separate steps. Images δs are given analytically by solving a linear system, and L1-functional are solved using shrinkage formulae. To perform the split, we include $d_x = \nabla_x, d_y = \nabla_y, d_z = \nabla_z, d_t = \nabla_t$So equation (12) becomes

$$\begin{aligned} &\left(\delta s^{k+1}, d_x, d_y, d_z, d_t\right) \\ &\quad = arg \min_{\delta s, d_x, d_y, d_z, d_t} \left\|\left(d_x, d_y, d_z\right)\right\|_1 \\ &\quad + \left\|d_t\right\|_1 + \frac{\mu}{2}\left\|\tilde{A}\delta s - \delta T^k\right\|_2^2 \\ &\quad \text{st.} \quad d_i = \nabla_i \delta s \end{aligned} \quad (14)$$

Constraints in equation (14) can be handled using the Bregman iteration as above, which leads to an iterative scheme.

III. EXPERIMENTAL RESULTS

A. Static experiments

The imaging performance was tested through various experimental configurations in terms of 3D static and dynamical imaging. This section presents, at first, results and experimental analysis on static experimental configurations. Then, quantitative indications on suspension characterisation are presented by conducting static experiments with water/sucrose suspensions.

Eight cases were conducted using cylindrical plastic objects in different combinations and positions with static objects. Objects of 10- 20- and 30-mm diameter have been tested. Any object less than 20 mm was difficult to reconstruct as the sensors could not be sensitive to those. In this work, cases with 20- and 30mm objects are presented. Various combinations of these objects were tested. Fig. 4(a) presents experimental photos of all the conducted experiments, (b) presents the reconstructed volumetric data by using cross-sectional slices and (c) presents the reconstructed volumetric data by isosurfaces, imposing 3D travel-time tomography. At first, simple tests with the single object at the center of ROI were

executed, distinguishing well between a 20- and 30mm object. Items were being positioned at different distances from each other. The variety and amount of different topologies in total applied offers a great indication of the system's overall spatial resolution and potential in industrial processes.

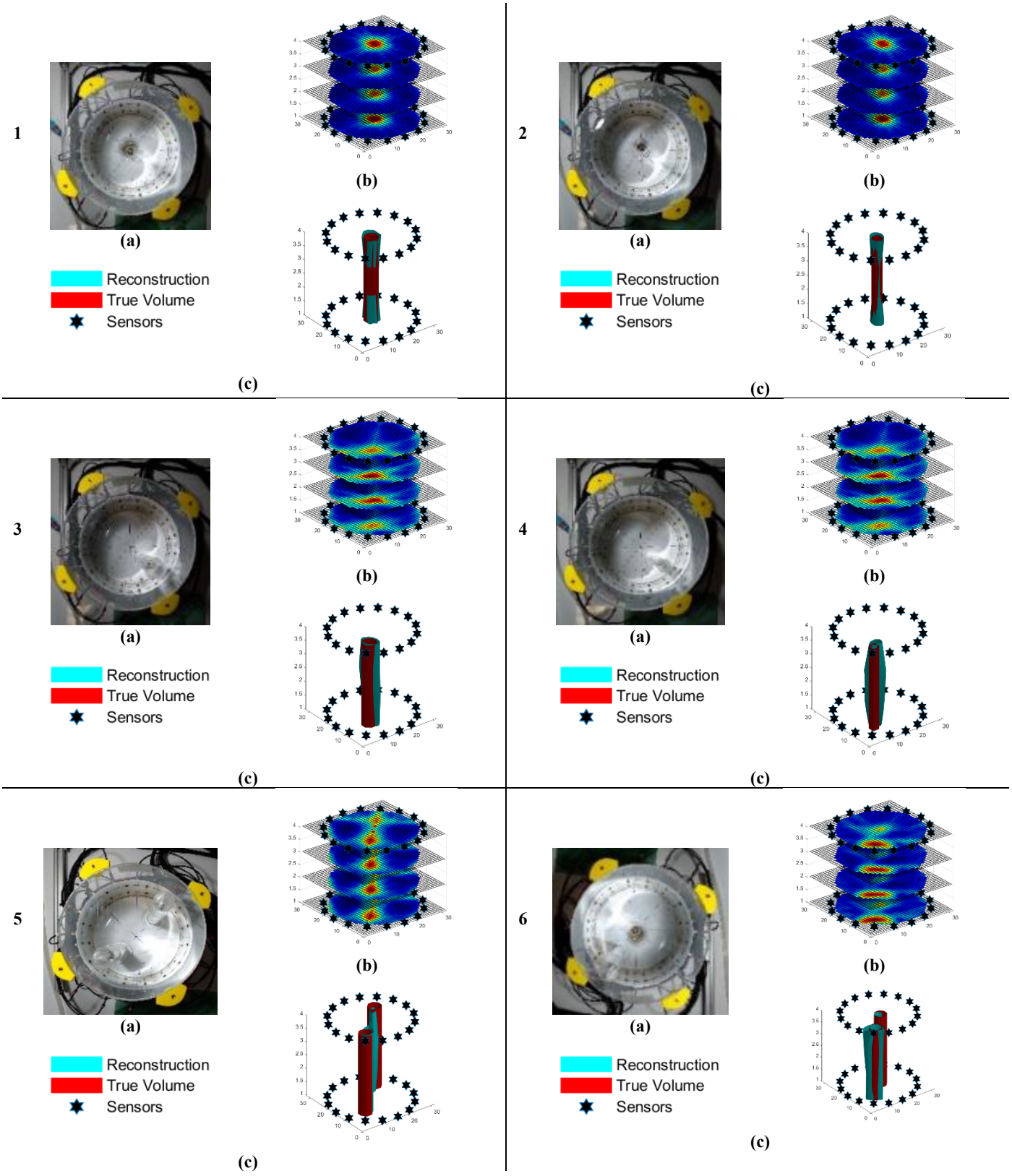

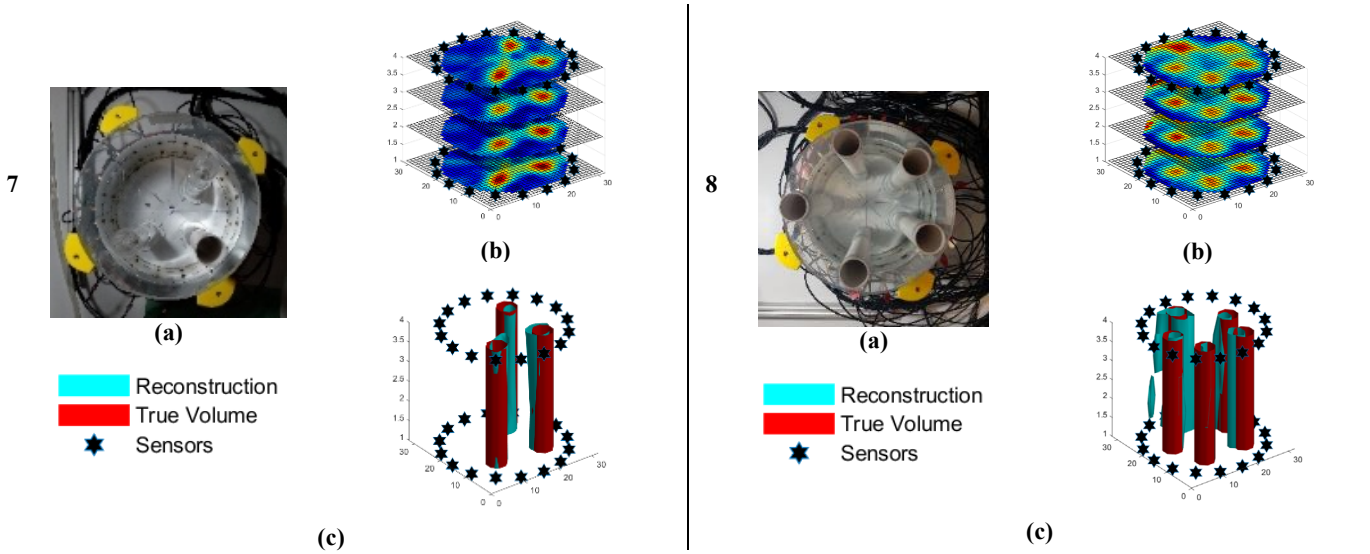

Fig. 4. Eight positions of single and multiple circular static objects of 30 and 20 mm diameter. **(a)** True positions **(b)** volumetric reconstructions with cross-sectional slices **(c)** volumetric reconstructions of isosurfaces.

A version of the structural similarity index (SSIM) based on volumetric data has been used [44] to acquire a quantitative index for the reconstructions. The SSIM is an image quality assessment metric that overall outperforms the error sensitivity-based image quality assessment techniques such as mean squared error (MSE) and peak signal-to-noise ratio (PSNR) [45]. A more advanced form of SSIM, called Multiscale SSIM (MS-SSIM), is conducted over multiple scales through a process of multiple stages of sub-sampling [46]. This image quality metric has been shown equal or better performance than SSIM on different subjective image and video databases. Thus, it is considered a more robust method for image quality assessment. In this work, MS-SSIM was used. MS-SSIM is presented:

$$MS-SSIM = [l_M(\delta s_{true}, \delta s_{rec})]^{a_M} \prod_{j=1}^{M} [c_j(\delta s_{true}, \delta s_{rec})]^{\beta_j} [s_j(\delta s_{true}, \delta s_{rec})]^{\gamma_j} \quad (15)$$

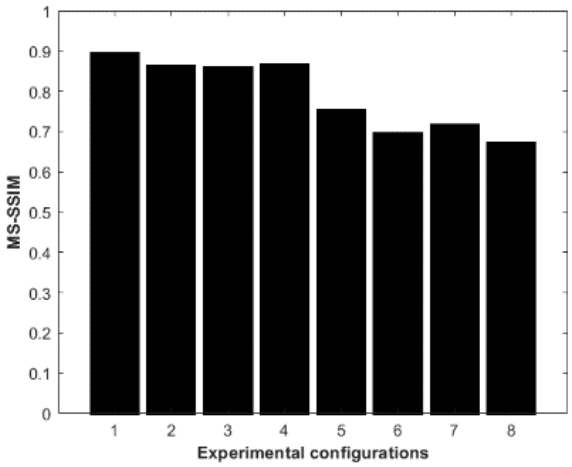

Fig. 5. MS-SSIM values for all the 8 experimental configurations with static cylindrical objects.

where δs_{true} and δs_{rec} are the 3D signals to compare, namely the true and the reconstructed volume; a_M, β_j and γ_j are the weighted parameters to define the importance of the three components l accounting for luminance, c accounting for contrast and s accounting for structural similarity. A higher MS-SSIM shows better image quality, with the region of the possible values to be in [0 1]. Fig. 5 presents MS-SSIM values of the eight experimental cases' reconstructed data. The quality metrics provide consistency to the nature of the experiment. At first, relatively high values result from the first four cases containing single objects as inclusions. Then, in the multiple inclusions case, the MS-SSIM values show a noticeable decay which is expected.

Additionally, specific experiments based on different concentrations of fine sucrose particles in water were conducted. These experiments aimed to test the quantitative response of the system. Travel-time delays are assumed to remain at a minimum level when the medium is almost homogeneous. On the other hand, delays of sound travel-time are increased if the differences in density and structure of materials within the medium remain significant. TOF delays result from different imaging and are defined in Eq. (1).

In this case, reference data (background) were collected by scanning the tank filled with water. Single inclusions of 20%, 42% and 70% kg/m^3 mixtures were tested. Fig. 6(a) presents photos of the experimental setup with water/sucrose inclusions, and Fig. 6(b) shows each case's reconstructed volumetric data. The solutions filled plastic cups of 1-mm wall thickness. The thin wall of the plastic cup ensures ultrasonic wave transmissivity. In cases of 20% and 42%, the delays are negative as the difference data addresses. The scale of these two reconstructions introduces a quantification indication as the reconstruction scale's absolute values are increased. The increasing number of negative values defines the ultrasound

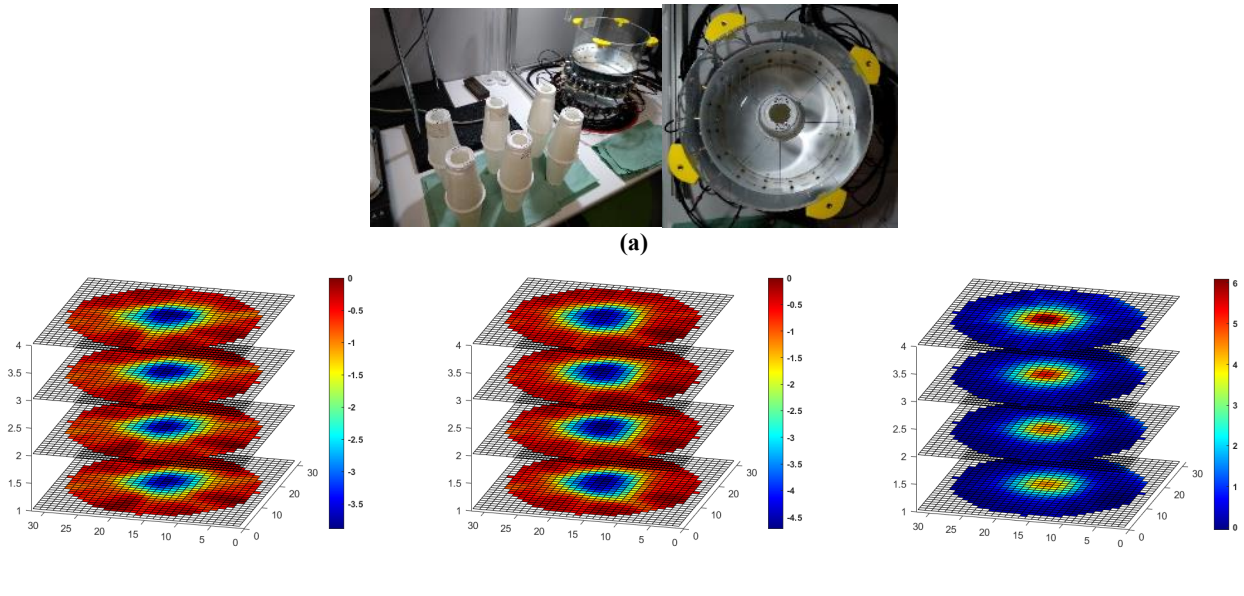

(a) **(b)** **(c)**

Fig. 6. (a) Photo of the experimental tank and of the inclusions filled with sucrose/water solutions **(b)** 20% **(c)** 42% **(d)** 70% kg/m^3 solutions' reconstructed volumes presented.

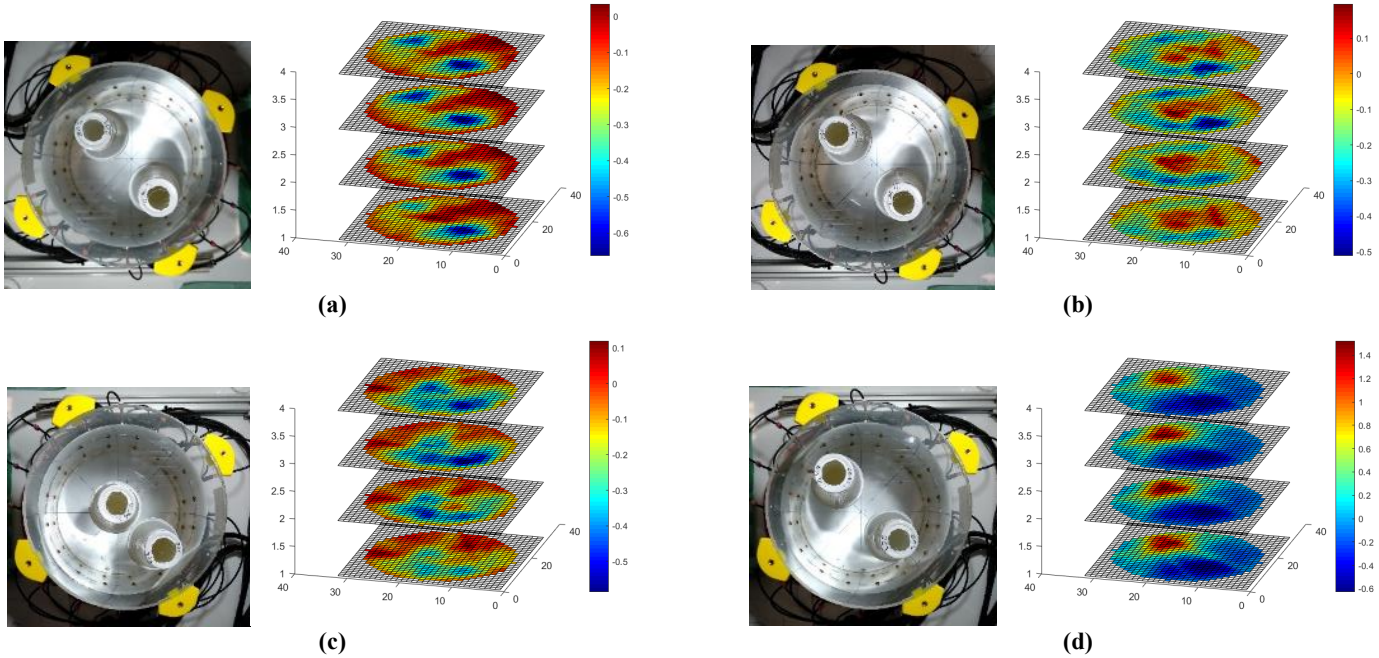

(a) **(b)** **(c)** **(d)**

Fig. 7. Multi-inclusions of sucrose/water solutions of **(a)** 20%-42% (b) 42%-50% far-positioned **(c)** 42%-50% near-positioned **(d)** 70%-20% kg/m^3. Figure includes experimental photos and reconstructed volumes.

acceleration within the tested liquid compared to the background. In the case of the 70%, the difference data are positive, and subsequently, the reconstruction includes positive TOF delays. Therefore, an opposite-colour bar reconstructed image than the previous cases were noticed.

This effect may come from the floating particles, as the mixture is a saturated solution, with its concentration being close to the saturation point of the mixture (66.7%). Therefore, the sound may be blocked by a significant number of undissolved particles, which will need more time to be dissolved or sediment. Difference data plots provide a good indication of quantification, as differences can be noticed in all three cases. Between the first two cases, the difference in negative data values indicates the inclusion density change, while few positive values come from noise in the measurements. On the other hand, in the third case of 70%, the higher positive values are established, showing the difference in medium's distributions

Continuing with the tests, multi-inclusion scenarios with concentrated solutions have been conducted. Four different combinations have been chosen to challenge the system's quantitative response in more depth. Same as before, the

60.78% case produced positive TOF delays, resulting in higher reconstructed values than the medium (water). However, this was the only case that decreased the sound propagation.

The difference between inclusion positioned simultaneously in the tank is evident in all the cases. Thus, the system provides relatively good substance characterisation incorporating a robust approach of travel-time imaging. Particular interest can be drawn by Fig. 7 (c), where the two inclusions of 42% and 50% concentration have been put very close to each other. In addition to the objects' location, their concentration is very close, too. Therefore, the case itself makes a special and challenging experiment. Nevertheless, the reconstruction is clear, indicating the concentrated regions of the medium. Moreover, one can notice a clear relation of the total cumulative sucrose concentration to the resulting scalebar of reconstructions amongst all the tests. They result in a clear indication of the quantitative travel-time imaging in concentrated solutions tests.

B. Dynamical experiments (4D)

This section presents results using the pre-described 4D regularization algorithm. Multiple frames have been used for reconstructions. The system was able to provide a high frame resolution of up to 4 frames per second. The system provides high temporal resolution as its electronic design can filter the waveform data and capture the TOF values of the first-arrival pulse, which saves much time from the data transferring process. Achieving such high temporal resolution regarding the UST system's limitations, we were able to test cases of real-time movement of objects. These tests can offer a first impression of real-time changes leading to a robust system for industrial tanks and pipes. The need of such a system is crucial as ultrasound process tomography gains more attention [47], [48], [49], [45].

A dynamical test was conducted incorporating a writing technique in 3D. This test aimed to efficiently produce a 3D letter of the English alphabet, tracking the individual generated frame's movement and superimposing them to a unified volume.

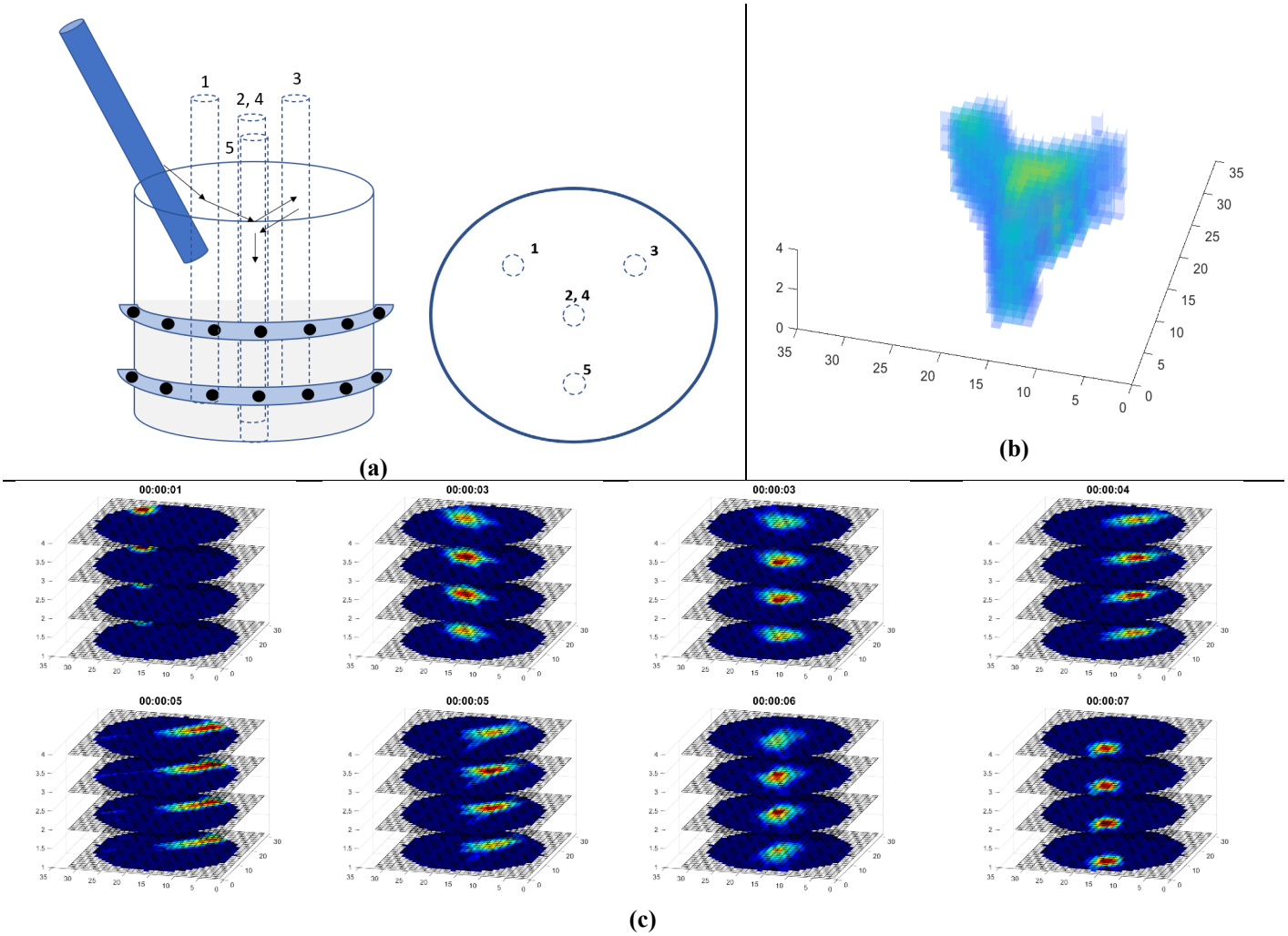

Fig. 8. Multi-frame 4D reconstruction of a moving plastic rod of 20-mm diameter, drawing the letter "Y". **(a)** Scheme describes the overall experiment and, more specifically, the motion of the plastic rod. The rod is inserted at the start of the process, at "00:00:03" reaches position "2", at "00:00:045" reaches position 3, at "00:00:06" is at position "4" and finally, at "00:00:07" reaches the last position "5". **(b)** Volumetric 4D reconstruction of the super-imposed volume depicting the engraved letter. **(c)** Individual volumetric frames presented with the respected times.

A plastic rod of 20 mm in diameter, acting as a writing object, was used. The pen is manually shifted inside the tank to produce the shape of a 3D letter. Fig. 8(a) displays a planar and a panoramic scheme describing the experiment. At first, the object is inserted into the tank. Then a motion begins driving the object linearly into 5 different spots of the tank, shaping letter "Y". Fig 8(c) displays 4D volumetric reconstructions of different frames with the respected times, and finally, Fig. 8(b) presents the reconstructed letter "Y". The reconstructed letter results from the individual superimposed frames into a unified volume. The resulting volume constitutes all the motion of the rod in the tank and defines the engraved letter.

In Fig. 9 the mean values of TOF delays have been presented. In contrast to the previous experiment, the TOF data starts from zero values as the tank's medium is homogeneous at the beginning, and after the insertion of the object, the values start increasing. During the small object' movement, a decrease in TOF delays has been recognised. Thus, it seems that the object's movement is not preventing the pulse's transmission as a static object would. Reconstructed isosurfaces have been displayed in this graph to highlight the rod's insertion frames and the 5 different spots of its movement inside the tank. A 4D approach to image reconstruction captures the 3D frame in their natural dynamical situation, providing a seamless method for motion tracking in tank reactors.

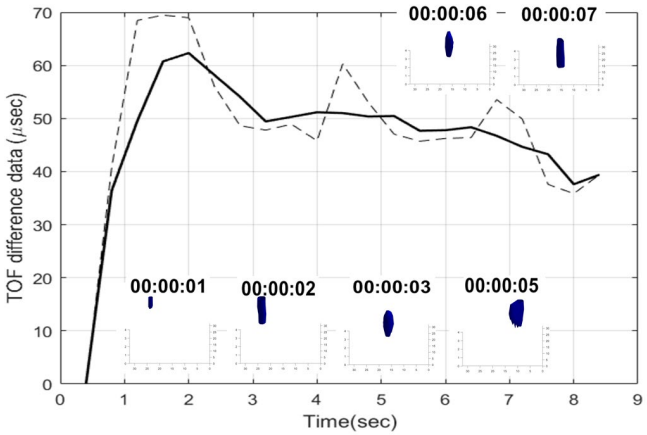

Fig. 9. Mean values of difference TOF data displayed together with reconstructed isosurfaces.

C. Crystallisation imaging

A reactive calcium carbonate crystallisation is applied in a batch concept. Fig. 10 shows the entire experimental setup in which the UST system is utilised to conduct process monitoring. The crystallisation reactor is made of plexiglass with an inner diameter of 190 mm. In the micron-sized, liquid-liquid crystallisation system, aqueous CO_3^{2-} as the reagent solution flows through an inlet pipe (diameter: 2 mm) into the crystalliser containing calcium chloride. A detailed description of the membrane contactor-based CO2 capture unit and its integration with a calcium carbonate crystallisation process is given in [50] and [51], respectively.

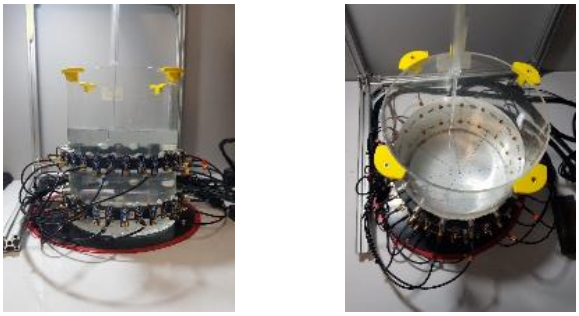

Fig. 10. Planar and panoramic photos of the crystallisation experimental apparatus.

The chemical reaction governing the crystallisation of calcium carbonate is presented in Eq. 16:

$$CO_3^{2-}{}_{(aq)} + 2NA^{+}_{(aq)} \rightarrow CaCO_{3\,(aq)} \downarrow + 2NaCl_{(aq)} \qquad (16)$$

Ultrasound transmission-based tomographic measurements are used to detect localised crystalline suspensions and monitor the reactive crystallisation of the calcium carbonate process. Other works proposed the use of the reflection measurements to detect the localised forming suspensions by incorporating machine learning techniques [52]. In the investigated crystallisation experiments, the initial concentration of calcium chloride is 1.6 g /L; the feed flow rate is 27 ml/min. Feed solution composition is NaOH at pH 12.1 ± 0.05 and CO_3^{2-} concentration of 0.14 ± 0.02 mol/L. Due to the fast kinetic nature of the particulate system, the nucleation phenomena are instantaneous, resulting in the formation of micron-sized particles. The ultrasonic excitation of 400kHz is not sensitive enough to react significantly to the onset of inherently stochastic nucleation, which begins at approximately 30 seconds after the first recorded frame of the process. After initiating the feed solution, the formation of amorphous calcium carbonate (ACC) could be an alternative cause of the TOF delay. Due to these delays, the system can display the injection point and the gradual increase of concentration/ suspension density at this specific point.

Fig. 11 shows photos of the first minute of the process. The photo sequence describes the start of ACC formation and its gradual growth in the time window of approximately one minute. Fig. 11 presents six reconstructed volumes of the tank during this time window. The UST images depict the ACC's formation and propagation in the tank, as after a few seconds, its sediments slowly to the bottom of the tank. The white circle points to the injection point. 4D imaging responded well in the z dimension, too, as the layers depicted the axial difference over time. Nucleation is an important first step in crystallisation process. Due to the zero mixing conditions, the compounds' transformation happens slower, and instead of producing clear calcite, a mesostructured calcite product occurs. It is worth noting that the early part of the feed may not be clear in UST images due to the limited resolution expected by two rings of 16 channel sensors.

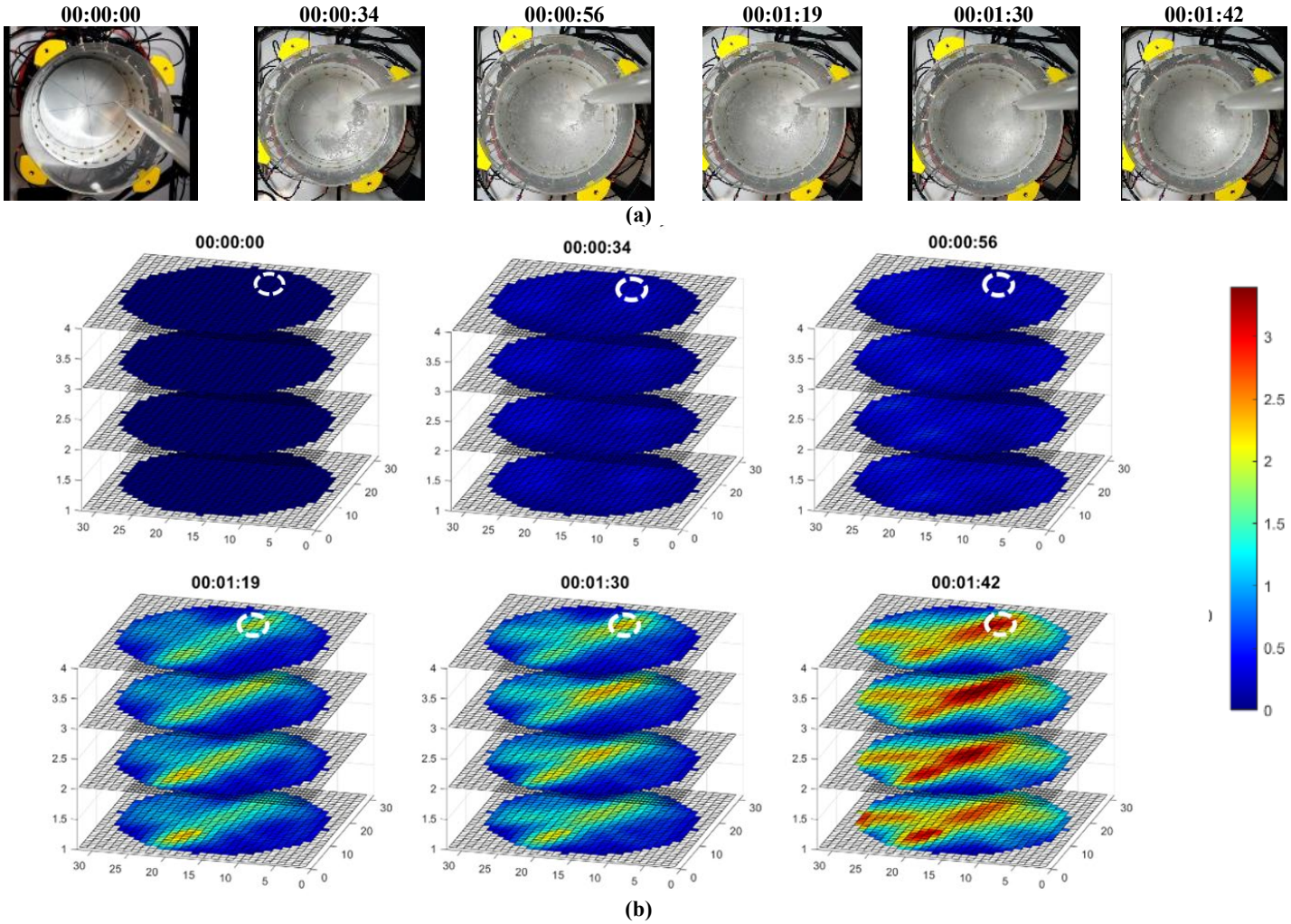

Fig. 11. **(a)** Experimental photos and **(b)** reconstructed frames presented regarding the case of 27 ml/min injection rate with no stirring over the first minute of the injection

Fig. 12 presents experimental photos of the whole experiment with a few corresponding frames. The sequence of the photos shows the progress of the medium's phase changes. Reconstructions are also presented in the specific times of the captured experimental photos. Reconstructions show the injection point and the propagation of denser suspension through the medium. Also, the homogeneity of the medium can be noticed from 37th minute and onwards appointed by the reconstructions. However, the injection point could still be visible as injection continuously runs and provide higher concentrations.

The following experiment was conducted with the same 27ml/min feeding rate and stirring using a flat-blade propeller with 100rpm were used. Crystalline forms of vaterite and calcite were produced, depending on the pH of the solution and the mixing conditions [53]. In the current precipitation system, there is a possibility for the following succession of the mechanism to occur [54], [55]: (i) the development and expansion of ACC; (ii) the ACC advancement and the surface complexation can lead to precipitation of the calcite ;(iii) further calcite expansion from ACC; (iv) more calcite surface complexation is created allowing for the further precipitation of calcite. Moreover, due to the nature of the experiment, lower concentration distributions are expected in the feeding region as stirring quickly dissolves and propagates the forming suspensions. Experimental photos of Fig. 13(a) confirm the theoretical background of the process. Compared to the no-stirring case, more clear polymorphs are formed, and the medium's phase is more dispersed with small micron-sized particles. According to the reconstructions in Fig. 13(b), no localised suspensions in the feeding region were noticed. On the other hand, the reconstructed volumes showed higher disturbances gradually increasing, reaching a peak and then decreasing again. These disturbances located at the center of the tank, around the stirring region. The disturbances define higher concentrations that occurred through the process as after a while start disappearing. Stirring finally dissolves them as depicted in reconstructions. Stirring also might be the reason for the high disturbances noticed at the centre of the tank. The crystalline formations move to the center and bottom of the ROI and finally, after frame "00:18:39" the TOF delays values start decreasing. The images are produced for every stage of the experiments. The UST images show the material phase changes during the crystallisation process.

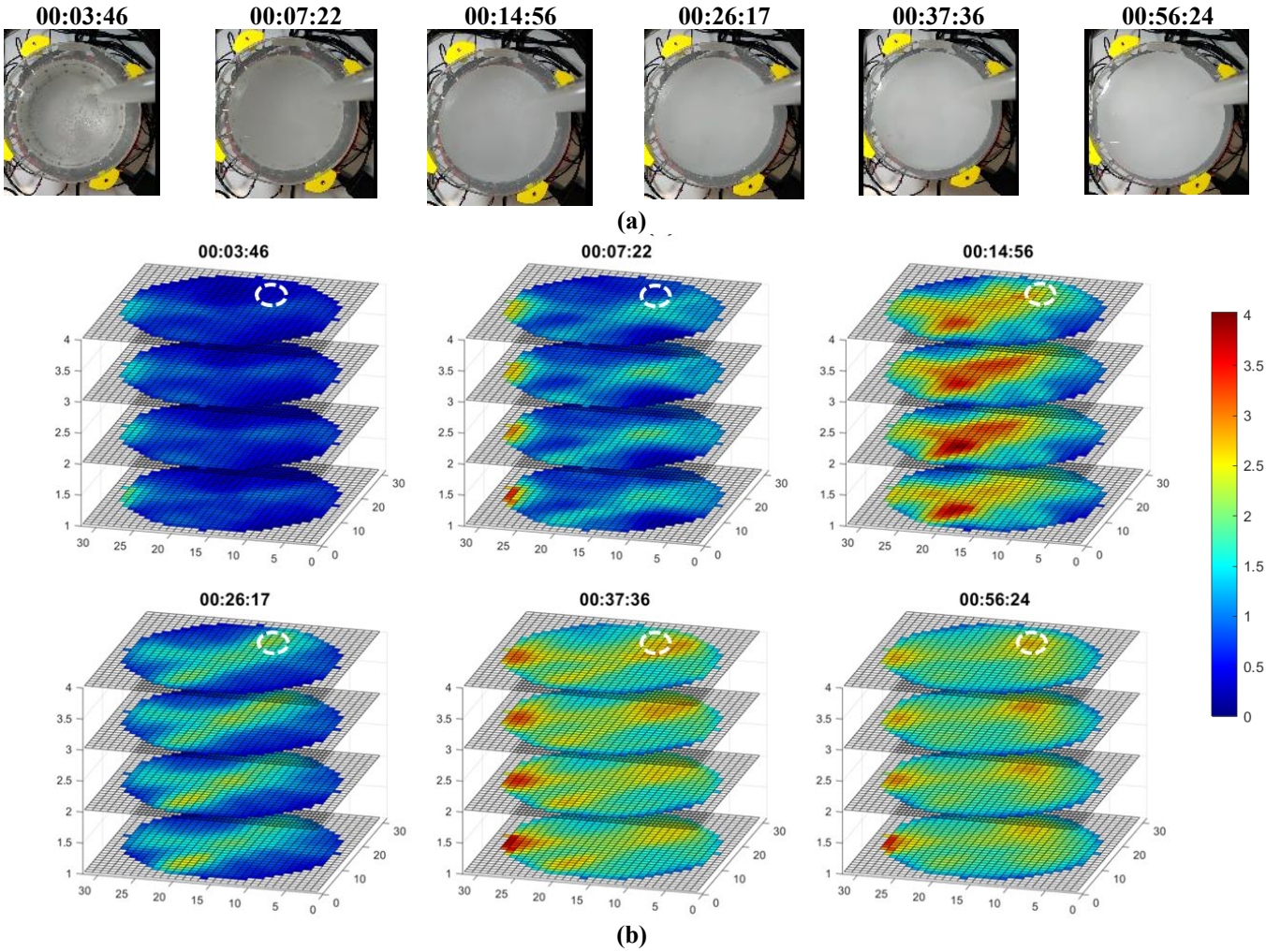

Fig. 12. **(a)** Experimental photos and **(b)** reconstructed frames presented regarding the case of 27 ml/min injection rate with no stirring.

The mean value data of UST are plotted, in Fig. 14, to show a global picture of the process dynamics. The rate of changes on these mean values will also give further insight into process dynamics. Two additional non-stirring experiments were undertaken using an 18ml/min and 27ml/min injection rate. Fig. 14 presents the mean value plots for the experimental cases using 18, 27 and 36 ml/min injection rates. In all the three graphs, the same pattern of first increasing and at some point, and after decreasing existence of TOF delays, can be recognised. The ε lines were used to depict the point at which the change of the function's direction happened. It is the point for every experiment when all the dense suspensions sediment to the bottom or dissolve to the tank's medium and TOF delays decrease. Comparing the ε_2, ε_3, and $\varepsilon_3$points, one can conclude the difference in the reaction between different injection rates. As higher is the injection rate, the quicker this point appears in the graphs. Because of the faster injection the chemical reaction forms faster and the maximum peak point always comes faster in time. Regarding the stirring and no-stirring crystallisation cases, the ε_1, ε_3 lines are compared. ε_1 maximum point comes faster than the ε_3, due to the high dynamics in stirring case. In stirring experiment, the ACC distributes and dissolves faster than in no-stirring cases. This aids to the uniformity of the medium and subsequently to lower TOF delays. Among all no-stirring crystallization cases, it was noticeable the decreasing effect of the mean values of TOF difference data after a specific point related to the rate of injection. The effects of stirring also were presented in the data.

IV. Conclusion

The 3D and 4D UST imaging for static and dynamical imaging are presented. In 3D imaging mode, the axial varying information can be extracted to provide unique information, which is not possible in traditional 2D imaging. For example, different behaviours in different z-axis positions in the crystallisation process are important in describing the process dynamics allowing for deriving additional information from axial variation in volumetric image. Separate two rings of 2D can give useful information on each level in the z-axis, but the 3D imaging by collecting inter-plan data that can also retrieve information for the volume between two rings of sensor giving a fully volumetric picture of the process under investigation.

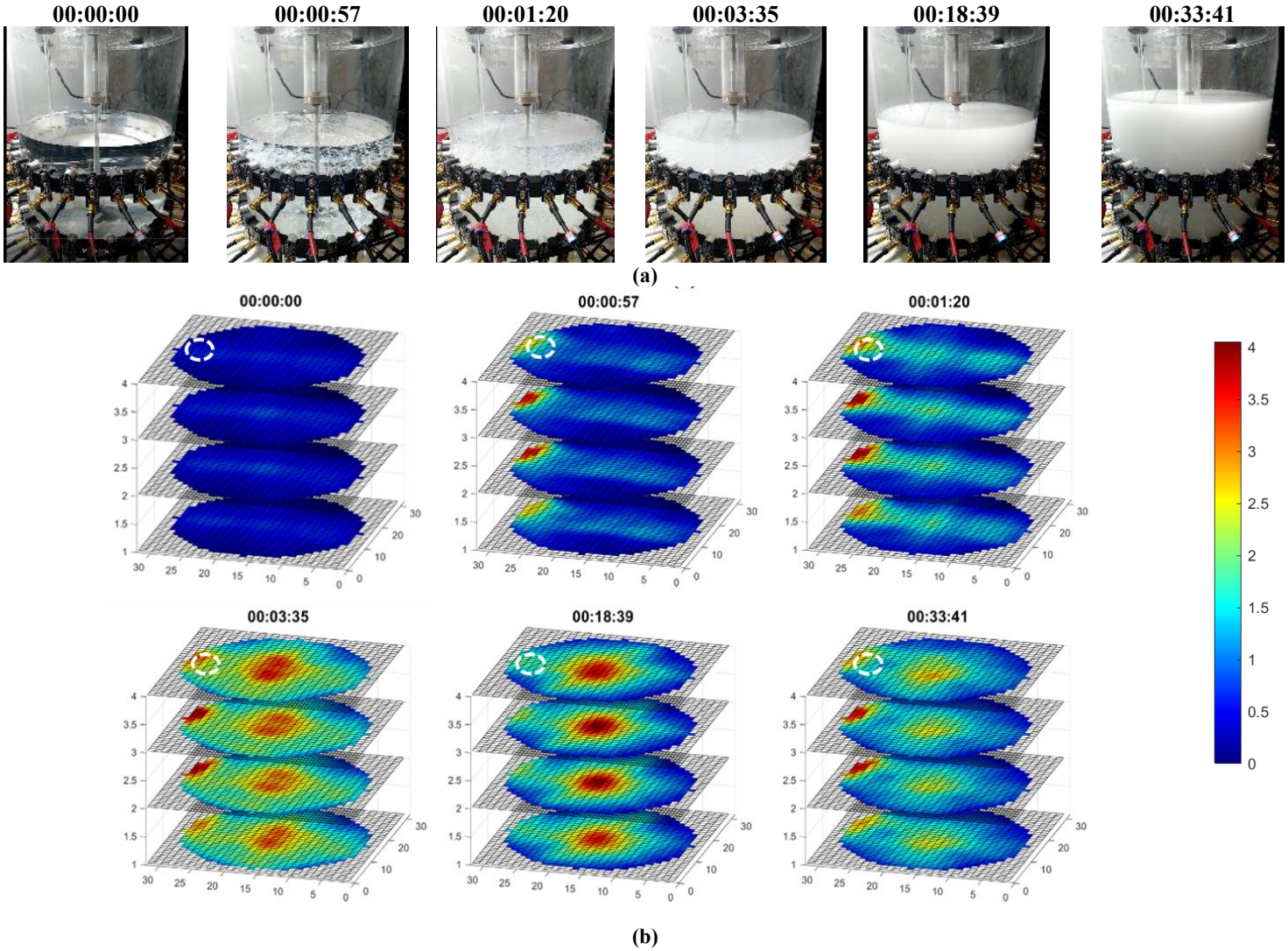

Fig. 13. **(a)** Experimental photos and **(b)** reconstructed frames presented regarding the case of 27ml/min injection rate and 100rpm stirring rate.

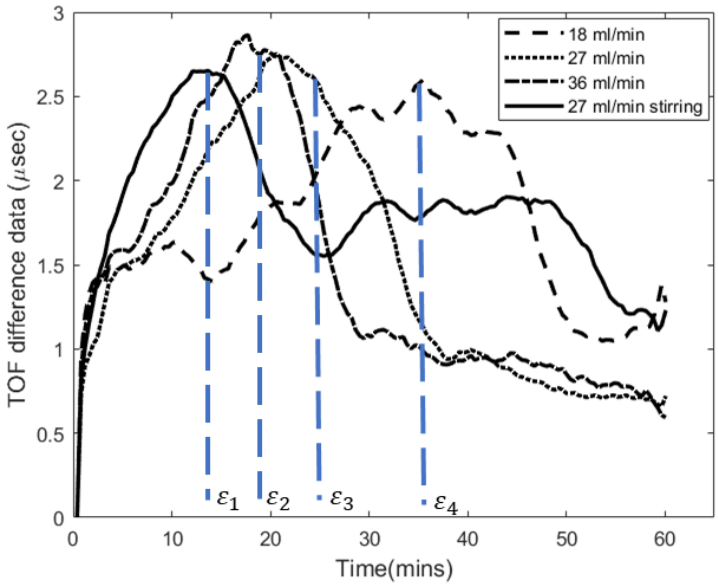

Fig. 14. Mean value plots of 36ml/min, 27ml/min and 18ml/min injection rate, all non-stirring. The mean value graph for the 27ml/min-100 rpm case is presented. A total 150 frames cover 60 minutes of the experiments

Additionally, the 4D implementation will further enhance the 3D imaging results by providing additional stabilities due to time-correlated data and time-correlated image regularization. The proposed method is applicable to the crystallisation process, where 4D crystallisation monitoring provides real-time information on feed points, mixing, process and crystal formation. This holistic time and space-based information then can be used to optimise the yield and avoid process malfunction.

REFERENCE

[1] B. Chen, J. F. P. J. Abascal, and M. Soleimani, "Electrical resistance tomography for visualization of moving objects using a spatiotemporal total variation regularization algorithm," *Sensors (Switzerland)*, vol. 18, no. 6, 2018.

[2] M. Soleimani, H. Wang, Y. Li, and W. Yang, "A Comparative Study of 3D Electrical Capacitance Tomography," *Int. J. Inf. Syst. Sci*, vol. 3, no. 2, pp. 292–306, 2007.

[3] A. Biguri, M. Dosanjh, S. Hancock, and M. Soleimani, "TIGRE: A MATLAB-GPU toolbox for CBCT image reconstruction," *Biomed. Phys. Eng. Express*, vol. 2, no. 5, 2016.

[4] P. Babin *et al.*, "Fast X-ray tomography analysis of bubble growth and foam setting during breadmaking," *J. Cereal Sci.*, vol. 43, no. 3,

pp. 393–397, 2006.

[5] M. Polacci *et al.*, “Crystallisation in basaltic magmas revealed via in situ 4D synchrotron X-ray microtomography,” *Sci. Rep.*, vol. 8, no. 1, Dec. 2018.

[6] R. Wajman, “The concept of 3D ECT system with increased border area sensitivity for crystallization processes diagnosis,” *Sens. Rev.*, vol. 41, no. 1, pp. 35–45, 2021.

[7] J. Wiskin *et al*., "Full Wave 3D Inverse Scattering Transmission Ultrasound Tomography: Breast and Whole Body Imaging," *2019 IEEE International Ultrasonics Symposium (IUS)*, 2019, pp. 951-958, doi: 10.1109/ULTSYM.2019.8925778.

[8] C. Liu, C. Xue, B. Zhang, G. Zhang, and C. He, “The application of an ultrasound tomography algorithm in a novel ring 3D ultrasound imaging system,” *Sensors (Switzerland)*, vol. 18, no. 5, May 2018.

[9] M. Birk, E. Kretzek, P. Figuli, M. Weber, J. Becker, and N. V. Ruiter, “High-Speed Medical Imaging in 3D Ultrasound Computer Tomography,” *IEEE Trans. Parallel Distrib. Syst.*, vol. 27, no. 2, pp. 455–467, Feb. 2016.

[10] H. Gemmeke and N. V. Ruiter, “3D ultrasound computer tomography for medical imaging,” *Nucl. Instruments Methods Phys. Res. Sect. A Accel. Spectrometers, Detect. Assoc. Equip.*, vol. 580, no. 2, pp. 1057–1065, 2007.

[11] J. Wiskin, D. T. Borup, S. A. Johnson, and M. Berggren, “Non-linear inverse scattering: High resolution quantitative breast tissue tomography,” *J. Acoust. Soc. Am.*, vol. 131, no. 5, pp. 3802–3813, May 2012.

[12] C. Li, L. Huang, N. Duric, H. Zhang, and C. Rowe, “An improved automatic time-of-flight picker for medical ultrasound tomography,” *Ultrasonics*, vol. 49, no. 1, pp. 61–72, Jan. 2009.

[13] C. Li, G. S. Sandhu, O. Roy, N. Duric, V. Allada, and S. Schmidt, “Toward a practical ultrasound waveform tomography algorithm for improving breast imaging,” *Med. Imaging 2014 Ultrason. Imaging Tomogr.*, vol. 9040, no. January 2015, p. 90401P, 2014.

[14] E. Miller, B. T. Cox, J. L. Herraiz, J. M. Udías, M. Pérez-Liva, and B. E. Treeby, “Time domain reconstruction of sound speed and attenuation in ultrasound computed tomography using full wave inversiona),” *J. Acoust. Soc. Am.*, vol. 141, no. 3, pp. 1595–1604, 2017.

[15] A. Javaherian, F. Lucka, and B. T. Cox, “Refraction-corrected ray-based inversion for three-dimensional ultrasound tomography of the breast,” *Inverse Probl.*, vol. 36, no. 12, 2020.

[16] A. Stanziola, S. R. Arridge, B. T. Cox, and B. E. Treeby, “A Helmholtz equation solver using unsupervised learning: Application to transcranial ultrasound,” *J. Comput. Phys.*, vol. 441, p. 110430, 2021.

[17] N. Li, L. Wang, J. Jia, and Y. Yang, “A Novel Method for the Image Quality Improvement of Ultrasonic Tomography,” *IEEE Trans. Instrum. Meas.*, vol. 70, 2021.

[18] K. Liu, B. Wu, C. He, N. Li, and K. Xu, “A Novel Sensitivity Matrix Construction Method for Ultrasonic Tomography Based on Simulation Studies,” *IEEE Trans. Instrum. Meas.*, vol. PP, pp. 1–15, 2019.

[19] M. Wang, C. Tan, and F. Dong, “Quantitative Sound Velocity Reconstruction Based on Ultrasonic Tomography,” no. 61973229, 2021.

[20] C. Tan, X. Li, H. Liu, and F. Dong, “An ultrasonic transmission/reflection tomography system for industrial multiphase flow imaging,” *IEEE Trans. Ind. Electron.*, vol. 66, no. 12, pp. 9539–9548, Dec. 2019.

[21] S. Langener, T. Musch, H. Ermert, and M. Vogt, “Simulation of full-angle ultrasound process tomography with two-phase media using a ray-tracing technique,” *IEEE Int. Ultrason. Symp. IUS*, pp. 57–60, 2014.

[22] N. A. Zulkiflli *et al.*, “Ultrasound Tomography Hardware System for Multiphase Flow Imaging,” *Proc. 2019 IEEE Int. Conf. Signal Image Process. Appl. ICSIPA 2019*, pp. 264–268, 2019.

[23] T. Rymarczyk and J. Sikora, “Applying industrial tomography to control and optimization flow systems,” *Open Phys.*, vol. 16, no. 1, pp. 332–345, 2018.

[24] M. H. F. Rahiman, R. A. Rahim, and Z. Zakaria, “Design and modelling of ultrasonic tomography for two-component high-acoustic impedance mixture,” *Sensors Actuators, A Phys.*, vol. 147, no. 2, pp. 409–414, Oct. 2008.

[25] M. Yang, H. I. Schlaberg, B. S. Hoyle, M. S. Beck, and C. Lenn, “Parallel Image Reconstruction in Real-Time Ultrasound Process Tomography for Two-phased Flow Measurements,” *Real-Time Imaging*, vol. 3, no. 4, pp. 295–303, Oct. 2002.

[26] F. Wiegand and B. S. Hoyle, “Simulations for Parallel Processing of Ultrasound Reflection-Mode Tomography with Applications to Two-Phase Flow Measurement,” *IEEE Trans. Ultrason. Ferroelectr. Freq. Control*, vol. 36, no. 6, pp. 652–660, 1989.

[27] S. Roux, L. Desbat, A. Koenig, and P. Grangeat, “Exact reconstruction in 2D dynamic {CT}: compensation of time-dependent affine deformations,” *Phys. Med. Biol.*, vol. 49, no. 11, pp. 2169–2182, May 2004.

[28] U. Schmitt and A. K. Louis, “Efficient algorithms for the regularization of dynamic inverse problems: I. Theory,” *Inverse Probl.*, vol. 18, no. 3, pp. 645–658, 2002.

[29] M. Soleimani, C. N. Mitchell, R. Banasiak, R. Wajman, and A. Adler, “Four-Dimensional electrical capacitance tomography imaging using experimental data,” *Prog. Electromagn. Res.*, vol. 90, no. January, pp. 171–186, 2009.

[30] G. Ma and M. Soleimani, “A versatile 4D capacitive imaging array: a touchless skin and an obstacle-avoidance sensor for robotic applications,” *Scientific Reports*, vol. 10, no. 1. 2020.

[31] V. Vishnevskiy, T. Gass, G. Szekely, C. Tanner, and O. Goksel, “Isotropic Total Variation Regularization of Displacements in Parametric Image Registration,” *IEEE Trans. Med. Imaging*, vol. 36, no. 2, pp. 385–395, 2017.

[32] Koulountzios, P.; Aghajanian, S.; Rymarczyk, T.; Koiranen, T.; Soleimani, M. An Ultrasound Tomography Method for Monitoring CO2 Capture Process Involving Stirring and CaCO3 Precipitation. *Sensors* 2021, *21*, 6995. https://doi.org/10.3390/s21216995 .

[33] V. V Krylov, “Geometrical acoustics approximation for Rayleigh and Lamb waves.”, PhD thesis, University of Loughborough , 2012.

[34] G. Marmitt, A. Kleer, I. Wald, H. Friedrich, and P. Slusallek, “Fast and accurate ray-voxel intersection techniques for iso-surface ray tracing,” *Vision, Model. Vis. 2004, VMV 2004 - Proc.*, no. January, pp. 429–435, 2004.

[35] J. Amanatides and A. Woo, “A Fast Voxel Traversal Algorithm for Ray Tracing,” *Eurographics*, vol. 87, no. 3, pp. 3–10, 1987.

[36] A. Majercik, C. Crassin, P. Shirley, and M. Mcguire, “A Ray-Box Intersection Algorithm and Efficient Dynamic Voxel Rendering,” *J. Comput. Graph. Tech. A Ray-Box Intersect. Algorithm*, vol. 7, no. 3, pp. 66–81, 2018.

[37] P. Koulountzios, T. Rymarczyk, and M. Soleimani, “Ultrasonic Tomography for automated material inspection in liquid masses,” *9th World Congr. Ind. Process Tomogr. WCIPT9, Sep 2018*, pp. 693–702, 2018.

[38] T. Rymarczyk, J. Sikora, P. Adamkiewicz, and K. Polakowski, “Effective ultrasound and radio tomography imaging algorithm for three-dimensional problems,” *2018 Appl. Electromagn. Mod. Tech. Med. PTZE 2018*, pp. 232–235, 2018.

[39] T. Rymarczyk, K. Kania, M. Gołąbek, J. Sikora, M. Maj, and P. Adamkiewicz, “Image reconstruction by solving the inverse problem in ultrasonic transmission tomography system,” *COMPEL - Int. J. Comput. Math. Electr. Electron. Eng.*, vol. 40, no. 2, pp. 238–266, 2020.

[40] P. Koulountzios, T. Rymarczyk, and M. Soleimani, “A quantitative ultrasonic travel-time tomography to investigate liquid elaborations in industrial processes,” *Sensors (Switzerland)*, vol. 19, no. 23, 2019.

[41] T. Rymarczyk, K. Polakowski, and J. Sikora, “a New Concept of Discretization Model for Imaging Improving in Ultrasound Transmission Tomography,” *Inform. Autom. Pomiary w Gospod. i Ochr. Środowiska*, vol. 9, no. 4, pp. 48–51, 2019.

[42] F. Li, J. F. P. J. Abascal, M. Desco, and M. Soleimani, “Total Variation Regularization with Split Bregman-Based Method in Magnetic Induction Tomography Using Experimental Data,” *IEEE Sens. J.*, vol. 17, no. 4, pp. 976–985, 2017.

[43] J. F. P. J. Abascal, P. Montesinos, E. Marinetto, J. Pascau, and M. Desco, “Comparison of total variation with a motion estimation based compressed sensing approach for self-gated cardiac cine MRI in small animal studies,” *PLoS One*, vol. 9, no. 10, 2014.

[44] E. P. Simoncelli, H. R. Sheikh, A. C. Bovik, and Z. Wang, “Image quality assessment: From error visibility to structural similarity,” *IEEE Trans. image Process.*, vol. 13, no. 4, pp. 600–612, 2004.

[45] C. L. Goh, R. A. Rahim, H. F. Rahiman, T. Zhen Cong, and Y. A. Wahad, “Simulation and experimental study of the sensor emitting

frequency for ultrasonic tomography system in a conducting pipe," *Flow Meas. Instrum.*, vol. 54, pp. 158–171, Apr. 2017.

[46] Z. Wang, E. P. Simoncelli and A. C. Bovik, "Multiscale structural similarity for image quality assessment," *The Thrity-Seventh Asilomar Conference on Signals, Systems & Computers, 2003*, 2003, pp. 1398-1402 Vol.2, doi: 10.1109/ACSSC.2003.1292216.

[47] T. Rymarczyk, G. Kłosowski, K. Kania, P. Rymarczyk, and M. Mazurek, "Tomographic ultrasonic sensors in industrial applications," *Prz. Elektrotechniczny*, vol. 97, no. 1, pp. 166–169, 2020.

[48] H. I. Schlaberg, M. S. Beck, B. S. Hoyle, C. Lenn, and Ming Yang, "Real-time ultrasound process tomography for two-phase flow imaging using a reduced number of transducers," *IEEE Trans. Ultrason. Ferroelectr. Freq. Control*, vol. 46, no. 3, pp. 492–501, 2002.

[49] H. I. Schlaberg, F. J. W. Podd, and B. S. Hoyle, "Ultrasound process tomography system for hydrocyclones," *Ultrasonics*, vol. 38, no. 1, pp. 813–816, 2000.

[50] S. Aghajanian, H. Nieminen, A. Laari, and T. Koiranen, "Integration of a calcium carbonate crystallization process and membrane contactor–based CO2 capture," *Sep. Purif. Technol.*, vol. 274, no. May, 2021.

[51] H. Nieminen, L. Järvinen, V. Ruuskanen, A. Laari, T. Koiranen, and J. Ahola, "Insights into a membrane contactor based demonstration unit for CO2 capture," *Sep. Purif. Technol.*, vol. 231, no. August 2019, p. 115951, 2020.

[52] D. Majerek *et al.*, "Machine Learning and Deterministic Approach to the Reflective Ultrasound Tomography," 2021.

[53] Q. Shen *et al.*, "Properties of amorphous calcium carbonate and the template action of vaterite spheres," *J. Phys. Chem. B*, vol. 110, no. 7, pp. 2994–3000, 2006.

[54] A. Lassin *et al.*, "Dynamics of calcium carbonate formation: Geochemical modeling of a two-step mechanism," *Geochim. Cosmochim. Acta*, vol. 240, pp. 236–254, 2018.

[55] D. Gebauer, A. Völkel, and H. Cölfen, "Stable prenucleation calcium carbonate clusters," *Science (80-.).*, vol. 322, no. 5909, pp. 1819–1822, 2008.

PANAGIOTIS KOULOUNTZIOS received the M.Eng. degree in electrical and computer engineering from the Technical University of Crete. He is currently pursuing the Ph.D. degree with the Engineering Tomography Laboratory (ETL). Since April 2018, he has been with ETL as Early Career Researcher (ESR) for Tomocon, an EU training network project. His Ph.D. is in ultrasound tomography for industrial process applications.

TOMASZ RYMARCZYK, Ph.D, D.Sc, Prof. He is the director in Research and Development Centre in Netrix S.A. and the director of the Institute of Computer Science and Innovative Technologies in the University of Economics and Innovation, Lublin, Poland. He worked in many companies and institutes developing innovative projects and managing teams of employees. His research area focuses on the application of non-invasive imaging techniques, electrical tomography, ultrasound tomography, radio tomography, image reconstruction, numerical modelling, image processing and analysis, process tomography, software engineering, knowledge engineering, artificial intelligence and computer measurement systems.

MANUCHEHR SOLEIMANI received the B.Sc. degree in electrical engineering and the M.Sc. degree in biomedical engineering, and the Ph.D. degree in inverse problems and electromagnetic tomography from The University of Manchester, Manchester, U.K., in 2005. From 2005 to 2007, he was a Research Associate with the School of Materials, The University of Manchester. In 2007, he joined the Department of Electronic and Electrical Engineering, University of Bath, Bath, U.K., where he was a Research Associate and became a Lecturer, in 2008, a Senior Lecturer, in 2013, a Reader, in 2015, and a Full Professor, in 2016. In 2011, he founded the Engineering Tomography Laboratory (ETL), University of Bath, working on various areas of tomographic imaging, in particular multimodality tomographic imaging. He has authored or co-authored well over 300 publications in the field.